

An examination of Homentropic Euler equations with Averaged Characteristics

Greg Norgard ^{*}and Kamran Mohseni[†]
University of Colorado, Boulder, Colorado, 80309, US

June 2, 2022

Abstract

The concept of employing averaged velocities in conservation laws is not a new one. This paper takes an approach and applies it to Homentropic Euler equations. The results are equations that we refer to as the Characteristically Averaged Homentropic Euler (CAHE) equations. This paper presents the derivation of the equations and an existence uniqueness proof for the derived equations. The speeds for shocks found in the CAHE equations are calculated. Solutions to the Riemann problem are examined analytically and numerically and are then compared to solutions of the Homentropic Euler equations.

1 Introduction

In the last several years, the Lagrangian Averaged Navier-Stokes Equations (LANS- α) have been showing promising results in modeling certain incompressible turbulent flows [1, 2, 3, 4, 5, 6, 7, 8, 9, 10]. Very simply put, this technique employs an averaged velocity and reduces the resolution required to resolve the flow. With work in this field making progress it is thought to be possible to employ an averaging technique successfully into compressible flow, thus modeling turbulence and shocks simultaneously.

As a beginning step the Burgers equation, $u_t + uu_x = 0$, was considered as it is a simplistic model of compressible flow. Multiple independent investigations were made into a modified Burgers equation with an averaged convective velocity [11, 12, 13, 14, 15],

$$u_t + \bar{u}u_x = 0 \tag{1a}$$

$$\bar{u} = g^\alpha * u \tag{1b}$$

$$g^\alpha = \frac{1}{\alpha} g\left(\frac{x}{\alpha}\right), \tag{1c}$$

^{*}Graduate Student, Department of Applied Mathematics.

[†]Associate Professor of Aerospace Engineering Sciences; Affiliated faculty in the Applied Mathematics Department.

where g is an averaging kernel. A brief summary of the primary results are as follows.

1. Solutions to Equations (1) exist and are unique [13, 11].
2. When the initial conditions are C^1 , the solution remains C^1 for all time [13].
3. For bell shaped initial conditions it was proven that as the averaging approaches zero ($\alpha \rightarrow 0$), the solutions to Equation (1) converge to the entropy solution of inviscid Burgers Equation [14].
4. There are a set of discontinuous initial conditions where solutions to Equation (1) will converge to a non-entropic solution, but these solutions are unstable [14, 12].
5. It is likely that solutions to Equation (1) will converge to the entropy solution of inviscid Burgers Equation for all continuous initial conditions, and thus the scheme

$$u_t + \bar{u}u_x = 0 \quad (2)$$

$$\bar{u} = g^\alpha * u \quad (3)$$

$$u(x, 0) = g^\alpha * u_0(x), \quad (4)$$

will converge to the entropy solution for any bounded initial condition u_0 [14].

Encouraged by these results, the next step is to attempt to introduce averaging into the 1D Homentropic Euler equations, a simplified version of the full Euler equations, where pressure is purely a function of density. There have been several attempts at such a regularization.

Using a Lagrangian averaging technique Bhat and Fetecau [16] derived the following equations

$$\rho_t + (\rho u)_x = 0 \quad (5)$$

$$w_t + (uw)_x - \frac{1}{2}(u^2 + \alpha^2 u_x^2)_x = -\frac{p_x}{\rho} \quad (6)$$

$$\rho w = \rho v - \alpha^2 \rho_x u_x \quad (7)$$

$$v = u - \alpha^2 u_{xx}. \quad (8)$$

While the solutions to the system remained smooth and contained much structure it was found that the equations were “not well-suited for the approximation of shock solutions of the compressible Euler equations.”

Another attempt by Bhat, Fetecau, and Goodman used a Leray-type averaging [17] leading to the equations

$$\rho_t + \bar{u}\rho_x + \rho u_x = 0 \quad (9)$$

$$u_t + \bar{u}u_x + \frac{p_x}{\rho} = 0 \quad (10)$$

$$u = \bar{u} - \alpha^2 \bar{u}_{xx}. \quad (11)$$

with $p = \kappa \rho^\gamma$. They then showed that weakly nonlinear geometrical optics (WNGO) asymptotic theory predicts the equations will have global smooth solutions for $\gamma = 1$ and form shocks in finite time for $\gamma \neq 1$.

Additionally in 2005, H. S. Bhat, R. C. Fetecau, J. E. Marsden, K. Mohseni and M. West [8] applied the Lagrangian averaging approach to the full compressible Euler equations. Their approach was successful in that the Lagrangian Averaged Euler (LAE- α) equations were derived. However, the equations were so intractable that they seemed impractical for real world applications.

This paper will examine yet another attempt at the regularization of the Homotropic Euler equations. Inspired by the existence uniqueness proofs from the averaged Burgers equations found in [13, 11], we averaged the characteristics of the Homotropic Euler equations to derive what we term as the Characteristically Averaged Homotropic Euler (CAHE) equations.

The following section follows the derivation and present the final equations. The existence and uniqueness of solutions to the equations are then proven in section 3. Sections 4 and 5 examine the speed of the shocks and solutions to the Riemann problem. Numerical simulations and their comparison to those of the Homotropic Euler equations are discussed in sections 6 and 7. The results are the briefly summarized in the concluding remarks.

2 Derivation of the equations

2.1 The Homotropic Euler equations

We begin the process of deriving the CAHE equations by starting with the Homotropic Euler equations. There are two equations to the Homotropic Euler equations. Conservation of mass and conservation of momentum. Pressure is expressed purely density raised to the power of γ .

$$\rho_t + (\rho u)_x = 0 \quad (12a)$$

$$(\rho u)_t + (\rho u u + \rho^\gamma)_x = 0 \quad (12b)$$

The equations are then written in primitive variable form

$$\begin{bmatrix} \rho \\ u \end{bmatrix}_t + \begin{bmatrix} u & \rho \\ \frac{a^2}{\rho} & u \end{bmatrix} \begin{bmatrix} \rho \\ u \end{bmatrix}_x = 0, \quad (13)$$

with $a^2 = \gamma \rho^{\gamma-1}$.

To get a clear view of the characteristics involved the equations are then diagonalized to obtain the equations

$$\begin{bmatrix} v^+ \\ v^- \end{bmatrix}_t + \begin{bmatrix} u+a & 0 \\ 0 & u-a \end{bmatrix} \begin{bmatrix} v^+ \\ v^- \end{bmatrix}_x = 0 \quad (14)$$

where

$$v^+ = u + \frac{2a}{\gamma - 1} \quad (15a)$$

$$v^- = u - \frac{2a}{\gamma - 1}. \quad (15b)$$

The variables v^\pm are commonly known as Riemann invariants. From Equation 14 it is easy to see that the quantity v^+ is convected at speed $u + a$ and v^- at speed $u - a$. Thus along the characteristics $u + a$, v^+ will remain constant.

Shocks will form when characteristics intersect. To prevent this from happening the characteristics are spatially averaged. This averaging is conducted by convoluting the variable to be averaged with an averaging kernel, g , and is represented by a bar above the variable. For example, the averaged velocity would be expressed

$$\bar{u} = g * u. \quad (16)$$

2.2 The Averaging Kernel

Several assumptions on the averaging kernel are made at this point. The kernel is assumed to be even, for isotropic purposes. For the purpose of Theorems 3.1 and 3.2 the kernel and its first derivative are assumed to be integrable. Of special interest is the Helmholtz filter which is defined as

$$u = \bar{u} - \bar{u}_{xx}, \quad (17)$$

and thus has an averaging kernel of

$$g(x) = \frac{1}{2} \exp(-|x|). \quad (18)$$

For all numerical simulations found in Sections 5, 6, and 7 the Helmholtz filter is used for its convenient inversion techniques.

Furthermore the kernel will be equipped with a parameter α which will control the amount of averaging. If g is the averaging kernel, then α is introduced as

$$g^\alpha = \frac{1}{\alpha} g\left(\frac{x}{\alpha}\right). \quad (19)$$

Thus as $\alpha \rightarrow 0$ the averaging kernel approaches the Dirac delta function.

2.3 Obtaining the CAHE Equations

Using the averaging kernel discussed above the characteristics of the Homentropic Euler equations are averaged to obtain the CAHE equations in diagonalized form.

$$\begin{bmatrix} v^+ \\ v^- \end{bmatrix}_t + \begin{bmatrix} \bar{u} + \bar{a} & 0 \\ 0 & \bar{u} - \bar{a} \end{bmatrix} \begin{bmatrix} v^+ \\ v^- \end{bmatrix}_x = 0. \quad (20)$$

Change the equations back into the primitive variable form and we get the equations

$$\rho_t + \bar{u}\rho_x + \rho \frac{\bar{a}}{a} u_x = 0 \quad (21a)$$

$$u_t + \bar{u}u_x + \frac{a\bar{a}}{\rho} \rho_x = 0 \quad (21b)$$

$$\bar{u} = g * u \quad (21c)$$

$$\bar{a} = g * a \quad (21d)$$

with $a^2 = \gamma\rho^{\gamma-1}$.

These are now the equations that will be examined for the rest of this paper and are referred to as the Characteristically Averaged Homentropic Euler (CAHE) equations. We begin by proving that Equations (21) have one and only one solution.

3 Existence and Uniqueness Theorem

A critically important property for the Equations (21) to have is that a solution exists. This section addresses this problem by presenting a proof for the existence and uniqueness of solutions. This proof uses a method of characteristics approach and is very similar to the existence uniqueness proof of Convectively Filtered Burgers equation found in [13]

An outline of the proof is as follows. Due to the nature of the equations, the fluid velocity and the speed of sound remain bounded. Since those speeds remain bounded, the first derivative of the averaged speeds will remain bounded as well. The characteristics are governed by the averaged speeds and with the first derivatives bounded, the characteristics may grow closer, but will never intersect. Thus the solution can be fully realized by the characteristics and the initial conditions.

Theorem 3.1 *Let $g(\mathbf{x}) \in W^{1,1}(\mathbb{R})$ and $u_0(x), a_0(x) \in C^1(\mathbb{R})$, then there exists a unique global solution $u(x, t), a(x, t) \in C^1(\mathbb{R}, \mathbb{R})$ to the initial value problem*

$$\rho_t + \bar{u}\rho_x + \rho \frac{\bar{a}}{a} u_x = 0 \quad (22a)$$

$$u_t + \bar{u}u_x + \frac{a\bar{a}}{\rho} \rho_x = 0 \quad (22b)$$

$$\bar{u} = g * u \quad (22c)$$

$$\bar{a} = g * a \quad (22d)$$

$$u(x, 0) = u_0 \quad (22e)$$

$$a(x, 0) = a_0 \quad (22f)$$

with $a^2 = \gamma\rho^{\gamma-1}$.

Proof Express Equations (22a) and (22b) with matrices as

$$\begin{bmatrix} \rho \\ u \end{bmatrix}_t + \begin{bmatrix} \bar{u} & \rho \frac{\bar{a}}{a} \\ \frac{a\bar{a}}{\rho} & \bar{u} \end{bmatrix} \begin{bmatrix} \rho \\ u \end{bmatrix}_x = 0 \quad (23)$$

By diagonalizing the matrix these equations can be rewritten as

$$\begin{bmatrix} v^+ \\ v^- \end{bmatrix}_t + \begin{bmatrix} \bar{u} + \bar{a} & 0 \\ 0 & \bar{u} - \bar{a} \end{bmatrix} \begin{bmatrix} v^+ \\ v^- \end{bmatrix}_x = 0. \quad (24)$$

It is here that we shift our perspective to a method of characteristics type view. Associate the maps ϕ^\pm with the characteristics of v^\pm . Thus we have

$$\frac{\partial}{\partial t} \phi^+(\xi, t) = \bar{u}(\phi^+(\xi, t), t) + \bar{a}(\phi^+(\xi, t), t) \quad (25)$$

$$\frac{\partial}{\partial t} v^+ = 0 \quad \text{along a } \phi^+ \text{ characteristic} \quad (26)$$

and

$$\frac{\partial}{\partial t} \phi^-(\xi, t) = \bar{u}(\phi^-(\xi, t), t) - \bar{a}(\phi^-(\xi, t), t) \quad (27)$$

$$\frac{\partial}{\partial t} v^- = 0 \quad \text{along a } \phi^- \text{ characteristic} . \quad (28)$$

From this we can obtain the estimates that

$$\|v^\pm(x, t)\|_{L^\infty} = \|v^\pm(x, 0)\|_{L^\infty} . \quad (29)$$

If the mappings ϕ^\pm have continuously differentiable inverses, φ^\pm , then Equation (24) has the solution

$$v^\pm(x, t) = v_0^\pm(\varphi^\pm(x, t)). \quad (30)$$

Sufficient conditions for such inverses to uniquely exist is if the Jacobians of ϕ^\pm are non-zero for all positions and time. Thus if $J(\phi^\pm) \neq 0$, Equation (24) is uniquely solved by (30).

For the next section of the proof we will be dealing with ϕ^+ . The results for ϕ^- follow in precisely the same manner. Since we are dealing with 1D the Jacobian of ϕ^+ is essentially ϕ_x^+ . It is clear from Equation (25) to see that the time derivative of ϕ_x^+ is

$$\frac{\partial}{\partial t} \phi_x^+ = (\bar{u}_x + \bar{a}_x) \phi_x^+. \quad (31)$$

Thus we see that

$$\phi_x^+ = \phi_x^+(0) \exp \left(\int_0^t \bar{u}_x + \bar{a}_x dt \right). \quad (32)$$

Thus ϕ_x^+ will remain non-zero if $\left| \int_0^t \bar{u}_x + \bar{a}_x dt \right| < \infty$.

First we will show that $u, a \in L^\infty$. We see that

$$\|2u\|_{L^\infty} = \left\| \frac{2a}{\gamma-1} + u + u - \frac{2a}{\gamma-1} \right\|_{L^\infty} \quad (33)$$

$$\leq \|v^+\|_{L^\infty} + \|v^-\|_{L^\infty}. \quad (34)$$

Looking at Equation (29) and noting that $\|v^+\|_{L^\infty}$ and $\|v^-\|_{L^\infty}$ are bounded for all time, then $\|u\|_{L^\infty}$ is bounded for all time. Similarly you can bound the quantity $\|a\|_{L^\infty}$ for all time.

Given that $g(x) \in W^{1,1}(\mathbb{R})$, there exists $M \in \mathbb{R}$, such that

$$\left\| \frac{\partial}{\partial x} g \right\|_{L^1} \leq M < \infty. \quad (35)$$

Knowing that $\frac{\partial}{\partial x} g \in L^1$ and $u \in L^\infty$, we know that $\frac{\partial}{\partial x} \bar{u}$ exists and that

$$\frac{\partial}{\partial x} \bar{u} = \frac{\partial}{\partial x} g * u.$$

Similarly

$$\frac{\partial}{\partial x} \bar{a} = \frac{\partial}{\partial x} g * a.$$

Using Young's inequality we can bound the derivatives \bar{u}_x and \bar{a}_x . We get

$$\left\| \frac{\partial}{\partial x} \bar{u} \right\|_{L^\infty} \leq \left\| \frac{\partial}{\partial x} g \right\|_{L^1} \|u\|_{L^\infty} \leq M \|u\|_{L^\infty} \quad (36)$$

$$\left\| \frac{\partial}{\partial x} \bar{a} \right\|_{L^\infty} \leq \left\| \frac{\partial}{\partial x} g \right\|_{L^1} \|a\|_{L^\infty} \leq M \|a\|_{L^\infty}. \quad (37)$$

This leads directly to the bound

$$\left| \int_0^t \bar{u}_x + \bar{a}_x dt \right| < M (\|u\|_{L^\infty} + \|a\|_{L^\infty}) t \quad (38)$$

Thus for finite time, the Jacobian of ϕ^\pm remains uniquely invertible, with a continuously differentiable inverse and thus (30) is a unique $C^1(\mathbb{R}^n)$ solution to (24). A unique $C^1(\mathbb{R}^n)$ solution to (22) follows accordingly.

Theorem 3.2 *Let $g(\mathbf{x}) \in W^{1,1}(\mathbb{R})$ and $u_0(x), a_0(x) \in L^\infty(\mathbb{R})$, then there exists a unique global solution $u(x, t), a(x, t) \in L^\infty(\mathbb{R}, \mathbb{R})$ to the initial value problem*

$$\rho_t + \bar{u}\rho_x + \rho \frac{\bar{a}}{a} u_x = 0 \quad (39a)$$

$$u_t + \bar{u}u_x + \frac{a\bar{a}}{\rho} \rho_x = 0 \quad (39b)$$

$$\bar{u} = g * u \quad (39c)$$

$$\bar{a} = g * a \quad (39d)$$

$$u(x, 0) = u_0 \quad (39e)$$

$$a(x, 0) = a_0 \quad (39f)$$

Proof The proof is the same as for Theorem 3.1. ϕ^\pm still have unique continuously differentiable inverses, and the solution remains in the same form as Equation (30), but now lacks continuity due to the initial conditions.

It should be noted that different averagings can be used for \bar{u} and \bar{a} . The existence and uniqueness proof will hold as long as a bound on the first derivatives of \bar{u} and \bar{a} remains constant. This is noted as the type of averaging used will affect shock speed as noted in Section 4.

4 Shock speeds

One of the consequences of the previous sections is that for continuous initial conditions, the solution will remain continuous. Also for initial conditions with a discontinuity, that discontinuity will remain. There are no colliding characteristics. Thus the “shock” is really a discontinuity that is being convected. If there is a discontinuity in $v_0^+(x)$ then that discontinuity will travel at speed $\bar{u}(x^*) + \bar{a}(x^*)$, where x^* is the location of the discontinuity. Similarly, if there is a discontinuity in $v_0^-(x)$ then that discontinuity will travel at speed $\bar{u}(x^*) - \bar{a}(x^*)$.

Consider the case where there is a single jump discontinuity in v^+ , but otherwise constant.

$$v^+(x) = \begin{cases} v_l^+ & x < 0 \\ v_r^+ & x \geq 0 \end{cases} \quad (40)$$

$$v^-(x) = C. \quad (41)$$

This will lead to a jump discontinuity in u and in a .

With \bar{u} and \bar{a} defined as in Equations (22) and the filter g being even and $\int g = 1$ then the speed of the discontinuity in Equations (40) will be

$$s = \frac{u_l + u_r}{2} + \frac{a_l + a_r}{2} \quad (42)$$

where u_l, u_r, a_l and a_r are the limiting values of u and a .

Similarly, if the jump discontinuity existed only in v^- then the speed of the discontinuity would be

$$s = \frac{u_l + u_r}{2} - \frac{a_l + a_r}{2}. \quad (43)$$

With multiple discontinuities or with nonconstant values around the discontinuities, the values of \bar{u} and \bar{a} will not be as clearly defined. However, for small values of α the filter will not “see” as far and the values of \bar{u} and \bar{a} will be roughly the average of the values just to the left and right of the discontinuity.

4.1 Alternative Averagings and Shock Speeds

In the above calculation \bar{u} and \bar{a} were defined as

$$\bar{u} = g * u \quad (44)$$

$$\bar{a} = g * a. \quad (45)$$

These are not, however, the only two ways of averaging u and a . Two possible alternatives that come readily are using a density weighted average of u

$$\bar{u} = \frac{g * (\rho u)}{g * \rho} \quad (46)$$

or and average of a based on the average of density

$$\bar{a}^2 = \gamma(g * \rho)^{\gamma-1}. \quad (47)$$

These alternatives will not affect the existence uniqueness theorems established in section 3. They will, however, change the shock speeds established earlier.

If Equation (46) is used the speed of a discontinuity in v^+ will travel at

$$s = \frac{\rho_l u_l + \rho_r u_r}{\rho_l + \rho_r} + \frac{a_l + a_r}{2}. \quad (48)$$

If Equation (47) is used then the speed of the same discontinuity would be

$$s = \frac{u_l + u_r}{2} + \sqrt{\gamma} \left(\frac{\rho_l + \rho_r}{2} \right)^{\frac{\gamma-1}{2}}. \quad (49)$$

Needless to say, how one chooses to define \bar{u} and \bar{a} will affect the speed of the discontinuities.

5 Riemann Solutions

This section builds upon the results of section 4 and establishes properties of the solutions of the CAHE equations for the Riemann problem. It then continues on to examine solutions of the CAHE equations if, instead of the Riemann problem, the initial conditions are slightly perturbed.

5.1 Riemann problem

Looking at Equation (30), it is clear that any discontinuity that exists in the initial condition remains in the solutions for all time. Furthermore, no additional discontinuities will form.

For the Riemann problem, at time $t = 0$ a single discontinuity will exist at the origin.

$$u(x, 0) = \begin{cases} u_l & x < 0 \\ u_r & x \geq 0 \end{cases} \quad (50)$$

$$a(x, 0) = \begin{cases} a_l & x < 0 \\ a_r & x \geq 0 \end{cases} \quad (51)$$

which can also be rewritten in terms of the variables v^+ and v^- .

$$v^+(x, 0) = \begin{cases} v_l^+ & x < 0 \\ v_r^+ & x \geq 0 \end{cases} \quad (52)$$

$$v^-(x, 0) = \begin{cases} v_l^- & x < 0 \\ v_r^- & x \geq 0 \end{cases} \quad (53)$$

These discontinuities will travel at the speeds discussed in section 4. We denoted the locations of the discontinuities in v^+ and v^- as x^- and x^+ . The speeds of these discontinuities are determined by

$$\frac{\partial}{\partial t}x^\pm = \bar{u}(x^\pm) \pm \bar{a}(x^\pm). \quad (54)$$

Clearly the discontinuity found in v^+ will travel at a faster speed than the discontinuity in v^- . Thus the solution will consist of three different areas separated by the locations of x^- and x^+ . The solution is then

$$v^+(x, t) = \begin{cases} v_l^+ & x < x^+(t) \\ v_r^+ & x^+(t) \leq x \end{cases} \quad (55)$$

$$v^-(x, t) = \begin{cases} v_l^- & x < x^-(t) \\ v_r^- & x^-(t) \leq x \end{cases} \quad (56)$$

If expressed in primitive variables the solution is

$$u(x, 0) = \begin{cases} u_l & x < x^-(t) \\ u_m & x^-(t) \leq x < x^+(t) \\ u_r & x^+(t) \leq x \end{cases} \quad (57a)$$

$$a(x, 0) = \begin{cases} a_l & x < x^-(t) \\ a_m & x^-(t) \leq x < x^+(t) \\ a_r & x^+(t) \leq x \end{cases} \quad (57b)$$

where $u_m = \frac{v_l^+ + v_r^-}{2}$ and $a_m = \frac{\gamma-1}{2} \frac{v_l^+ - v_r^-}{2}$.

Thus in general, the Riemann problem will produce the solutions Equations (57) where two discontinuities will propagate dependent upon the speeds of the averaged velocity and speed of sound. If the initial conditions happen to be chosen, such that v^+ or v^- are constant, then there will exist only one traveling discontinuity. The following subsection show numerical simulations of a typical Riemann solution.

5.1.1 Riemann solution Numerics

To find the solution (57), the values $u_{l,m,r}$ and $a_{l,m,r}$ are all known, one simply has to determine the location of x^\pm . This is easily enough done by using Equation (54). A typical iteration is as follows.

1. The values of $u(x, t_1)$ and $a(x, t_1)$ are known on a uniform grid.
2. The Helmholtz operator is then numerically inverted to give the values of \bar{u} and \bar{a} on the uniform grid. These values are then interpolated to give the values of $\bar{u} \pm \bar{a}$ at x^\pm .
3. The positions of the x^\pm , are then advanced in time by the values of $\bar{u} \pm \bar{a}$ on x^\pm calculated in the previous step.

4. The values of $u(x, t_2)$ and $a(x, t_2)$ are now known using Equation (57) and current positions of x^\pm .

The inversion of the Helmholtz operator is described in Section 6.

To examine a typical case, we will simulate the Riemann solution with the initial conditions

$$u(x, 0) = \begin{cases} 0 & x < 0 \\ 0 & x \geq 0 \end{cases} \quad (58a)$$

$$a(x, 0) = \begin{cases} 2 & x < 0 \\ 1 & x \geq 0 \end{cases} \quad (58b)$$

This set of initial conditions will be referred to as Example 1a. This is a standard shock tube problem where the velocity is zero initially and there is a jump in pressure. The initial conditions can be seen in Figure 1. With these values there are discontinuities in variables v^+ and v^- . These discontinuities are seen to propagate to the right and left respectively as seen in Figure 2. These numerical simulations were conducted with resolution 2^{10} with $\alpha = 0.02$.

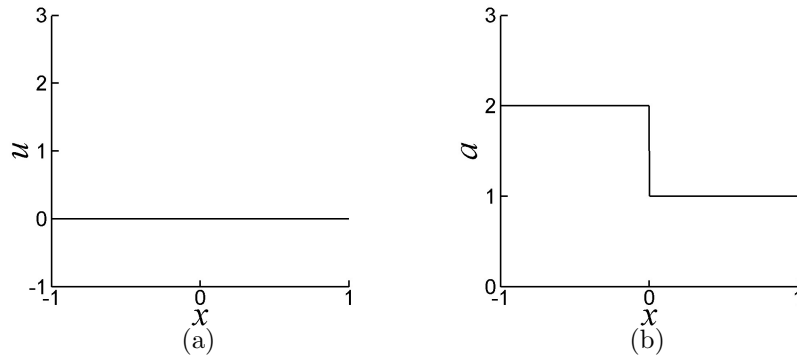


Figure 1: The initial conditions for the Riemann problem. (a) The initial velocity profile is $u = 0$. (b) The initial speed of sound profile is a simple jump discontinuity, indicating a higher pressure on the right.

5.2 The Perturbed Riemann Problem

While the solution to the Riemann problem generally leads to one or two traveling discontinuities, we have found that some of these traveling discontinuities are unstable.

There have been examinations of the Burgers equation with the characteristics averaged [13, 14, 11, 12]. In two of these papers it was seen that certain traveling discontinuities in these equations were unstable and if perturbed would become expansion waves [14, 12]. We have found similar behavior for the CAHE equations.

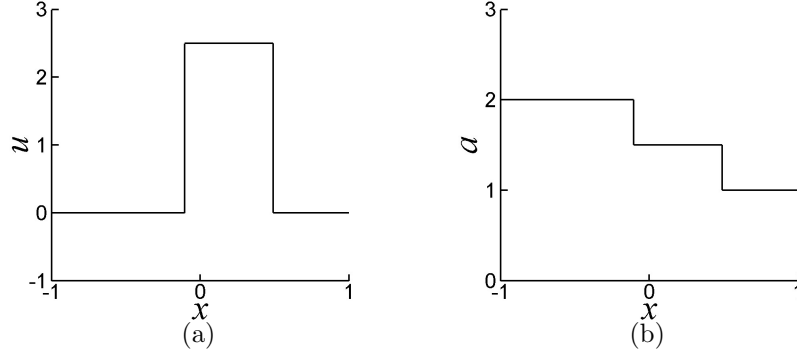


Figure 2: The solution to the Riemann problem with initial conditions Equation (58). There are two shocks found in both the velocity and speed of sound. This is the solution at time $t = 0.2$

Consider Example 1a as seen in Figure 2. The position of the leftmost shock is denoted x^- . The value of $u - a$ is greater to the right of x^- than it is to the left. So clearly $\bar{u} - \bar{a}$ is increasing across the discontinuity at x^- . Thus the v^- characteristics are diverging there. This is typically indicative of an expansion wave. However, the spreading of this discontinuity remains simply a discontinuity.

Suppose instead that instead of a strict discontinuity, the function was a continuous function, albeit extremely steep. The diverging characteristics would then spread this extremely steep gradient and gradually make it less steep, forming an expansion wave. Thus, this traveling discontinuity is unstable, and any amount of smoothing would lead to an expansion wave as opposed to a shock.

Using numerics discussed in section 6, we made runs using the same initial conditions as in Example 1a except the initial conditions were initially “smoothed”, using the same Helmholtz filter as employed in the averaging of the characteristics. We will refer to this as Example 1b. This smoothing of the initial conditions is similar to the approach used in [14]. Figure 3 shows the initial conditions where the smoothing is readily apparent in the a variable. Figure 4 shows the solution at time $t = 0.2$. The right shock remains unchanged from the unperturbed solution seen in Figure 2. However, an expansion wave is clearly seen on the left in the perturbed solution where previously there was a discontinuity. These simulations were run with a resolution of 2^{10} grid points and $\alpha = 0.02$.

To summarize, the Riemann problem is easily enough solved, and produces one or two traveling discontinuities, some of which may be unstable. If instead the discontinuities in the initial conditions are replaced with steep, but continuous gradients, then the results will begin to include expansion waves in addition to the shocks.

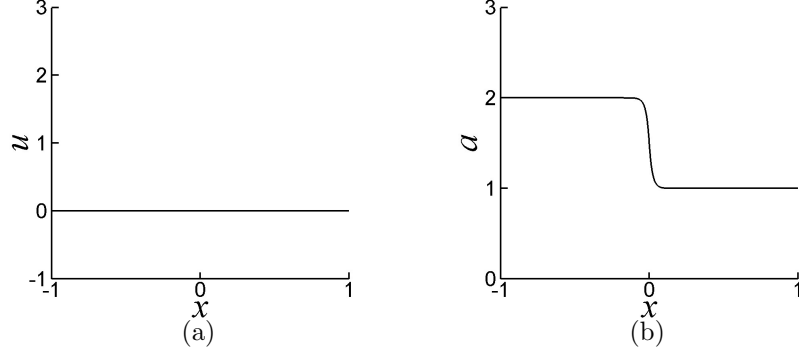


Figure 3: The initial conditions for the perturbed Riemann problem. (a) The initial velocity profile is $u = 0$. (b) The initial speed of sound profile is a smoothed pressure jump.

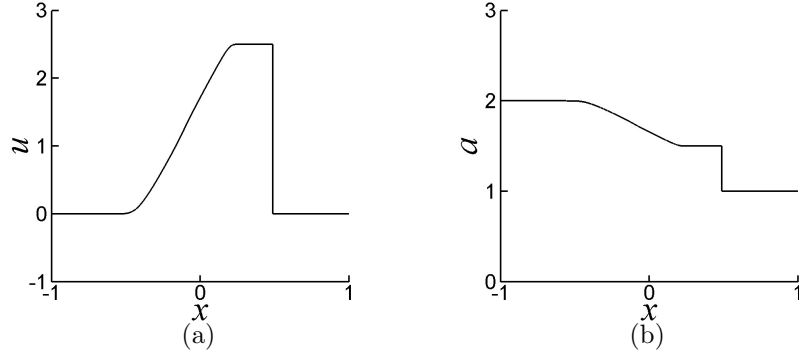


Figure 4: The solution to the perturbed Riemann problem. The initial conditions are Equation (58) that have been filtered with the Helmholtz filter. There is clearly a shock and an expansion wave. This is the solution at time $t = 0.2$.

6 Numerics

In section 7 we will compare the behavior of the CAHE equations to the homentropic Euler equations. To accomplish this we are going to use a numerical technique based on the inherent structure of the CAHE equations. This technique is very similar in nature to that used by Bhat and Fetecau [12]. Since the equations we are investigating are inspired by the use of averaged characteristics, our numerical method will track the characteristics as they evolve in time.

Our numerical method is interested in solving Equations 21 with initial con-

ditions

$$v^+(x, 0) = v_0^+(x) \quad (59)$$

$$v^-(x, 0) = v_0^-(x). \quad (60)$$

Since we cannot operate on an infinite domain we restrict the problem to the domain $[a, b]$ and assume that on the boundaries

$$\frac{\partial}{\partial x} v^+(x, t) = 0 \quad (61)$$

$$\frac{\partial}{\partial x} v^-(x, t) = 0. \quad (62)$$

From Equations (25) and (27) we know that the value of v^\pm doesn't change along its characteristics, thus

$$v^\pm(\phi^\pm(X)) = v_0^\pm(X), \quad (63)$$

Where X is the label of the characteristic.

Let \mathbf{x} be the equally spaced grid points on the interval $[-a, a]$. Let \mathbf{X}^\pm be the positions of the characteristics X_i . These vector can also be considered as the values of ϕ or as a dynamic grid. At time $t = 0$, $\mathbf{x} = \mathbf{X}^+ = \mathbf{X}^-$. Notationally let $v^\pm(\mathbf{x})$ be a vector containing the values of v^\pm evaluated at points \mathbf{x} and let $v^\pm(\mathbf{X}^\pm)$ be v^\pm evaluated at the locations of the characteristics \mathbf{X}^\pm .

The positions of the characteristics are iterated in time, thus giving us the solution. A typical iteration proceeds as follows.

1. The values of $v^\pm(\mathbf{X}^\pm)$ are known and remain constant through time as a result of Equation 63. Using cubic splines these values are interpolated to $v^\pm(\mathbf{x})$.
2. From $v^\pm(\mathbf{x})$, it is a simple task of finding the values of u and a on the grid \mathbf{x} . The Helmholtz operator is then numerically inverted to give the values of \bar{u} and \bar{a} on \mathbf{x} . These values are then interpolated back to give the values of $\bar{u} \pm \bar{a}$ on \mathbf{X}^\pm .
3. The positions of the characteristics, \mathbf{X}^\pm , are then iterated in time by the values of $\bar{u} \pm \bar{a}$ on \mathbf{X}^\pm calculated in the previous step.

In step 2, the Helmholtz operator is numerically inverted. To give a brief explanation of how the operator is inverted first consider a finite difference approximation of a second derivative on a equispaced grid.

$$\frac{\partial^2}{\partial x^2} f(x(i)) = \frac{1}{12\Delta x} [-1f(x_{i-2}) + 16f(x_{i-1}) - 30f(x_i) + 16f(x_{i+1}) - 1f(x_{i+2})] \quad (64)$$

Thus the Helmholtz operator $(1 - \alpha^2 \frac{\partial^2}{\partial x^2})$ can be represented as a quintdiagonal matrix. This is easily inverted allowing the calculation of $\bar{u} \pm \bar{a}$ from $u \pm a$ on an equispaced grid.

A benefit to this method is that plotting the vectors \mathbf{X}^\pm versus time gives a graph of the characteristic plane.

7 Comparisons with Homentropic Euler equations

The CAHE equations were based on the Homentropic Euler equations so naturally we will compare the behavior of the two. In particular this section will examine two examples chosen specifically to compare and contrast the equations behavior. We consider two sets of initial conditions with the Homentropic Euler equations simulations marked as Examples 2a and 3a and the CAHE equations simulations marked as Examples 2b and 3b.

7.1 Numerics for Homentropic Euler

For the numerical simulations of the Homentropic Euler equations the Richtmyer method was utilized as described by [18]. This method is second order finite difference scheme and employs an artificial viscosity. Clearly this is not the most optimal numerical scheme for the Euler equations, but run at a sufficiently high resolution it will suit our purposes. For reference there were 2^{12} grid points and an artificial viscosity of $\nu = 0.08$ used on all runs for the Homentropic Euler equations.

7.2 Example 2

The first example was chosen so that the CAHE equations would have a single traveling shock. The initial conditions are

$$u(x, 0) = \begin{cases} 5 & x < 0 \\ 0 & x \geq 0 \end{cases} \quad (65a)$$

$$a(x, 0) = \begin{cases} 2 & x < 0 \\ 1 & x \geq 0 \end{cases} \quad (65b)$$

Notice that with these initial conditions there is a discontinuity in the variable v^+ , but v^- is constant. Since v^- is constant in the beginning it should remain constant for all time. This is a consequence of the fact that no characteristics are created or destroyed as time progresses.

Figure 5 shows the simulation for Example 2b. The simulation was conducted with a resolution of 2^{12} and $\alpha = 0.02$. Figures 5a and 5b show the single discontinuity progressing to the right as expected. Figures 5c and 5d show the values of v^+ and v^- . The discontinuity in v^+ has traveled to the right and as expected v^- remains constant.

Figures 5e and 5f show the paths of the v^+ and v^- characteristics respectively. Figure 5e shows that the characteristics of v^+ are moving towards each other and as they near the shock are bent toward each other. They do not, however, intersect. Figure 5f shows that the characteristics of v^- pass through the shock and upon doing so change their speed to match the characteristics on the other side.

Now we examine the behavior of Homentropic Euler equations for the same initial conditions. Figure 6 shows the simulation for Example 2a. The simulation was conducted with a resolution of 2^{12} .

Figures 6a and 6b show a shock progressing to the right as expected. In addition there is an expansion wave also occurring.

Figures 6c and 6d show the values of v^+ and v^- . The discontinuity in v^+ has traveled to the right. In v^- , we notice that while it was initially constant, it now has new values. Indeed, both the expansion wave and shock are shown in v^- .

Figures 6e and 6f are not graphs of the actual simulation. The Richtmyer method does not lend itself to characteristic graphs as does the method used for the CAHE equations. Instead they are sketches that depict the behavior of the giving simulation.

The characteristics in v^+ change speed as they travel through the expansion wave. The characteristics intersect causing the shock. Thus at the shock the characteristics are destroyed.

For the v^- characteristics, at time $t = 0$, the characteristics to the left of the discontinuity have a speed greater than those to the right, but both are less than the speed of the shock. The result is that the characteristics on the right will be absorb into the shock and between the characteristics on the left and the shock there will be a gap devoid of characteristics. This gap is filled with an expansion wave created at $t = 0$ and new characteristics that are created at the location of the shock continually as time progresses. The values of these new characteristics can be determined with the Rankine-Hugoniot jump conditions.

7.3 Example 3

The first example was chosen so that the CAHE equations would have a single traveling shock. The initial conditions are

$$u(x, 0) = \begin{cases} 0 & x < 0 \\ -9.37440483... & x \geq 0 \end{cases} \quad (66)$$

$$a(x, 0) = \begin{cases} 2 & x < 0 \\ 1 & x \geq 0 \end{cases} \quad (67)$$

First we examine the behavior of Homentropic Euler equations for Example 3a. Figure 7 shows the simulation for Example 3a. The simulation was conducted with a resolution of 2^{12} .

Figures 7a and 7b show a single shock. The shock is close to stationary but is progressing to the right.

Figures 7c and 7d show the values of v^+ and v^- . The discontinuity can be seen in both Riemann invariants. This is noticeably different than the behavior of the CAHE equations where a single traveling shock will appear in only one of the invariants.

Figures 7e and 7f are not graphs of the actual simulation. The Richtmyer method does not lend itself to characteristic graphs as does the method used

for the CAHE equations. Instead they are sketches that depict the behavior of the given simulation.

The v^+ characteristics to the left of the discontinuity travel faster than those to the right with the speed of the shock found in between those speeds. Thus the characteristics collide and cause the shock. The shock absorbs the characteristics.

The v^- characteristics to the left of the discontinuity travel faster than those to the right, however both are slower than the speed of the shock. Thus there is an area devoid of characteristics between the left characteristics and the shock. This is filled with new characteristics that originate from the shock.

Now we examine the CAHE equations for Example 3b. Notice that with these initial conditions there is a discontinuity in the both variables v^+ and v^- . Thus it is to be expected that there will be two phenomenon, either expansion waves or shocks. In this case, both will be shocks.

Figure 5 shows the simulation for Example 3b. The simulation was conducted with a resolution of 2^{12} and $\alpha = 0.02$.

Figures 5a and 5b clearly show two distinct shocks, even if they are close together, progressing to the left. These shocks can also be seen in Figures 5c and 5d in the variables v^+ and v^- .

Figures 5e and 5f show the paths of the v^+ and v^- characteristics respectively. The line across the center of the graph represents the remapping of characteristics as they had grown too close together for convenient computation. For both sets of characteristics there is a convergence of the characteristics towards the shock. This demonstrates that it is a stable discontinuity and that a perturbation will not turn these into expansion waves. Again the characteristics are bent towards each other, but never intersect.

7.4 Comparisons between the Homentropic Euler and the CAHE equations

From these examples and previous sections we can begin to draw comparisons between the Homentropic Euler equations and the CAHE equations.

Both sets of equations are capable of forming shocks and expansion waves from the Riemann problem. For Homentropic Euler equations it is well established that for the Riemann problem there will often be both a shock and an expansion wave formed. With the CAHE equations there will always be two shocks formed. However, if the initial conditions are slightly smoother, some of those discontinuities will be found to be unstable and result in an expansion wave. Thus both behaviors can be said to be found in both equations.

In terms of speed of the shocks, we have found there to be differences. In the Homentropic Euler equations, the speed of the shocks are determined by the Rankine-Hugoniot conditions, in order to preserve mass and momentum. With the CAHE equations the speed of a discontinuity is determined by the speed of the averaged characteristics at the location of the discontinuity. In section 4, it can be seen that with the averaging chosen for this paper that the shock speed differs from those of the Homentropic Euler equations. From this it is also clear

that while the Homentropic Euler equations may be formally regained from the CAHE equations by letting $\alpha \rightarrow 0$, the solution will not converge to weak solutions of the Homentropic Euler equations. It may be possible, however, to choose an averaging scheme such that the shock speeds between the two equations are the same or similar.

Additionally the conditions under which a single traveling shock differs between the two equations as is demonstrated in Examples 2 and 3. For a single shock to form with the CAHE equations either v^+ or v^- must be constant. Even if it were possible to find an averaging scheme such that the shock speeds between the two equations are the same, these conditions would not change. For the Homentropic Euler equations, the condition is tied in with the Rankine-Hugoniot conditions.

The final difference noted between these equations is significant. As seen in Examples 2 and 3, for the Homentropic Euler equations, there can be areas devoid of characteristics. These can be filled with expansion waves or by new characteristics originating from the shock. By averaging the characteristics in the CAHE equations, there will be no areas devoid of characteristics. Thus there will be no generation of new characteristics. This can cause significant differences in behavior as seen in Example 2, where v^- remains a constant for the CAHE equations, but not for the Homentropic Euler equations. This again is a property that is unaffected by the averaging scheme chosen.

8 Conclusions

The CAHE equations were derived by taking the Homentropic Euler equations and spatially averaging the characteristics. This led to a new set of equations that has many interesting properties. Existence and uniqueness proofs, Theorem 3.1 and 3.2, were proven by establishing that the characteristics of the equations never intersect. In the process this established that any initial conditions in $C^1(\mathbb{R})$ will have a solution in $C^1(\mathbb{R})$. Furthermore any discontinuities in the initial conditions will remain and be convected in the solution for all time.

The speeds of shocks in the CAHE equations were found to be determined by the speed of the characteristics at the location of those shocks. Furthermore, different averaging schemes were shown to provide different shock speeds.

The Riemann problem was then examined, where solutions were generally found to consist of two travel discontinuities. However, often one of the discontinuities can prove to be unstable and by smoothing the initial conditions will develop into an expansion wave instead.

Finally using some numerical examples and results from the previous sections the CAHE equations were compared and contrasted with the Homentropic Euler equation from which they originated. Both can generate shocks and expansion waves from the Riemann problem. With the averaging scheme employed in the paper, the speed of the shocks differ. For the examples chosen, the behavior of the equations proved to be significantly different. Finally, the Homentropic Euler equations showed the generation of new characteristics, while with the

CAHE equations, new characteristics will never be generated. From this it seems clear that as $\alpha \rightarrow 0$ the solutions to the CAHE equations will not converge to weak solutions of the Homentropic Euler equations.

The CAHE equations have proven to have convenient existence and uniqueness properties. When continuous initial conditions are chosen, the solution will remain continuous. However, the equations seem to display behavior with too significant of departure from the Homentropic Euler equations to be of use in gas dynamic applications.

References

- [1] A. Cheskidov, D.D. Holm, E. Olson, and E.S. Titi. On a Leray- α model of turbulence. *Royal Society London, Proceedings, Series A, Mathematical, Physical & Engineering Sciences*, 461(2055):629–649, 2004.
- [2] C. Foias, D. D. Holm, and E. S. Titi. The Navier-Stokes- α model of fluid turbulence. *Physica D.*, 152-3:505–519, 2001.
- [3] C. Foias, D.D. Holm, and E.S. Titi. The three dimensional viscous Camassa-Holm equations, and their relation to the Navier-Stokes equations and turbulence theory. *Journal of Dynamics and Differential Equations.*, 14(1):1–35, 2002.
- [4] J.E. Marsden and S. Shkoller. Global well-posedness of the LANS- α equations. *Proc. Roy. Soc. London*, 359:1449–1468, 2001.
- [5] K. Mohseni, B. Kosović, S. Shkoller, and J.E. Marsden. Numerical simulations of the Lagrangian averaged Navier-Stokes (LANS- α) equations for homogeneous isotropic turbulence. *Phys. Fluids*, 15(2):524–544, 2003.
- [6] H. Zhao and K. Mohseni. A dynamic model for the Lagrangian averaged Navier-Stokes- α equations. *Phys. Fluids*, 17(7):075106, 2005.
- [7] K. Mohseni, H. Zhao, and J. Marsden. Shock regularization for the Burgers equation. AIAA paper 2006-1516, 44th AIAA Aerospace Sciences Meeting and Exhibit, Reno, Nevada, January 9-12 2006.
- [8] H. S. Bhat, R. C. Fetecau, J. E. Marsden, K. Mohseni, and M. West. Lagrangian averaging for compressible fluids. *SIAM Journal on Multiscale Modeling and Simulation*, 3(4):818–837, 2005.
- [9] D.D. Holm, J.E. Marsden, and T.S. Ratiu. Euler-Poincaré models of ideal fluids with nonlinear dispersion. *Phys. Rev. Lett.*, 349:4173–4177, 1998.
- [10] S.Y. Chen, D.D. Holm, L.G. Margoin, and R. Zhang. Direct numerical simulations of the Navier-Stokes- α model. *Physica D*, 133:66–83, 1999.
- [11] H.S. Bhat and R.C. Fetecau. A Hamiltonian regularization of the Burgers equation. *J. Nonlinear Sci.*, 16(6):615–638, 2006.

- [12] H. S. Bhat and R. C. Fetecau. Stability of fronts for a regularization of the Burgers equation. *Quarterly of Applied Mathematics*, 66:473–496, 2008.
- [13] G. Norgard and K. Mohseni. A regularization of the Burgers equation using a filtered convective velocity. *J. Phys. A: Math. Theor.*, 41:1–21, 2008.
- [14] G. Norgard and K. Mohseni. Convergence of convectively filtered Burgers equation to the entropy solution of inviscid Burgers equation. unpublished, 2008. Also <http://arxiv.org/abs/0805.2176>.
- [15] D.D. Holm and M.F. Staley. Wave structures and nonlinear balances in a family of evolutionary PDEs. *SIAM J. Appl. Dyn. Syst.*, 2:323–380, 2003.
- [16] H. S. Bhat and R. C. Fetecau. Lagrangian averaging for the 1D compressible Euler equations. *Discrete and Continuous Dynamical Systems*, 6(5):979–1000, 2006.
- [17] H. S. Bhat, R. C. Fetecau, and J. Goodman. A Leray-type regularization for the isentropic Euler equations. *Nonlinearity*, 20:2035–2046, 2007.
- [18] Culbert B. Laney. *Computational Gasdynamics*. Cambridge University Press, 1998.

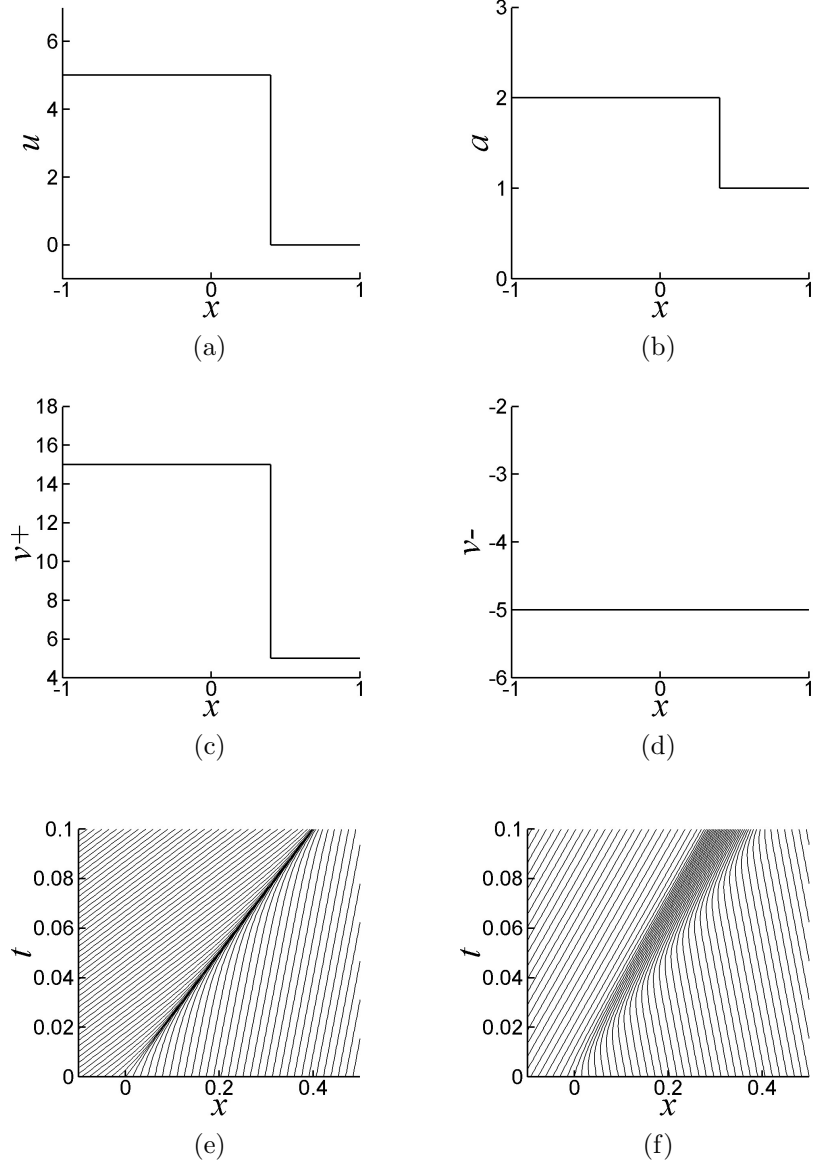


Figure 5: Example 2b at time $t = 0.1$. This example was chosen so that the CAHE equations would have a single traveling shock which is clearly visible in the velocity and speed of sound in (a) and (b). (c) and (d) show graphs of the Riemann invariants v^+ and v^- . Note that v^- is constant as it was in the initial conditions. (e) and (f) show the v^+ and v^- characteristics respectively. Notice that the v^+ characteristics are converging to the shock but never intersect, while the v^- characteristics pass through the shock and change speeds as they do so.

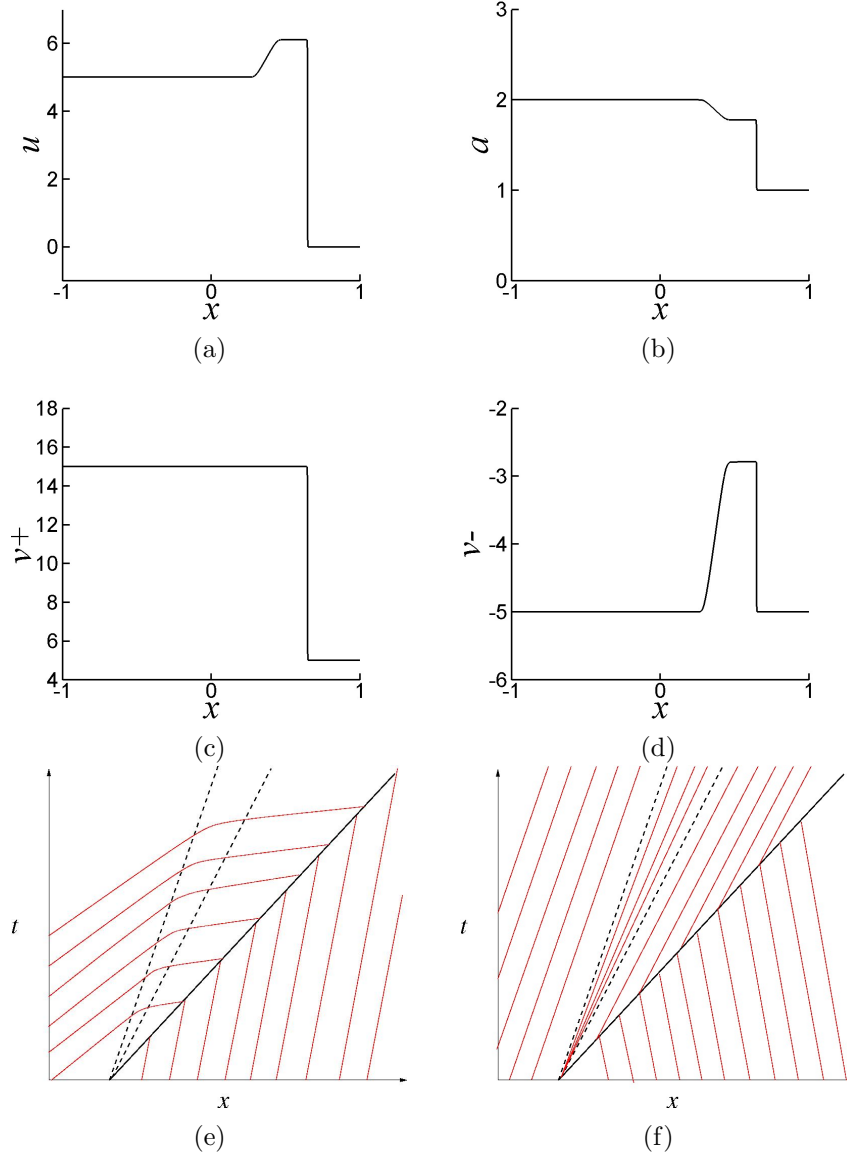


Figure 6: Example 2a at time $t = 0.1$. While the CAHE equations form a single shock the Homentropic Euler equations clearly form a shock and expansion wave. (a) and (b) show the shocks and expansion wave clearly in the velocity and speed of sound. (c) and (d) show the Riemann invariants v^+ and v^- . Notice that while v^- began as a constant it is no longer. This is due to the creation of new characteristics at the shock. (e) and (f) show sketches of the characteristics for this example. (e) shows that the v^+ characteristics are being absorbed by the shock. (f) shows the v^- characteristics being created at the shock. The dotted line represents the expansion wave.

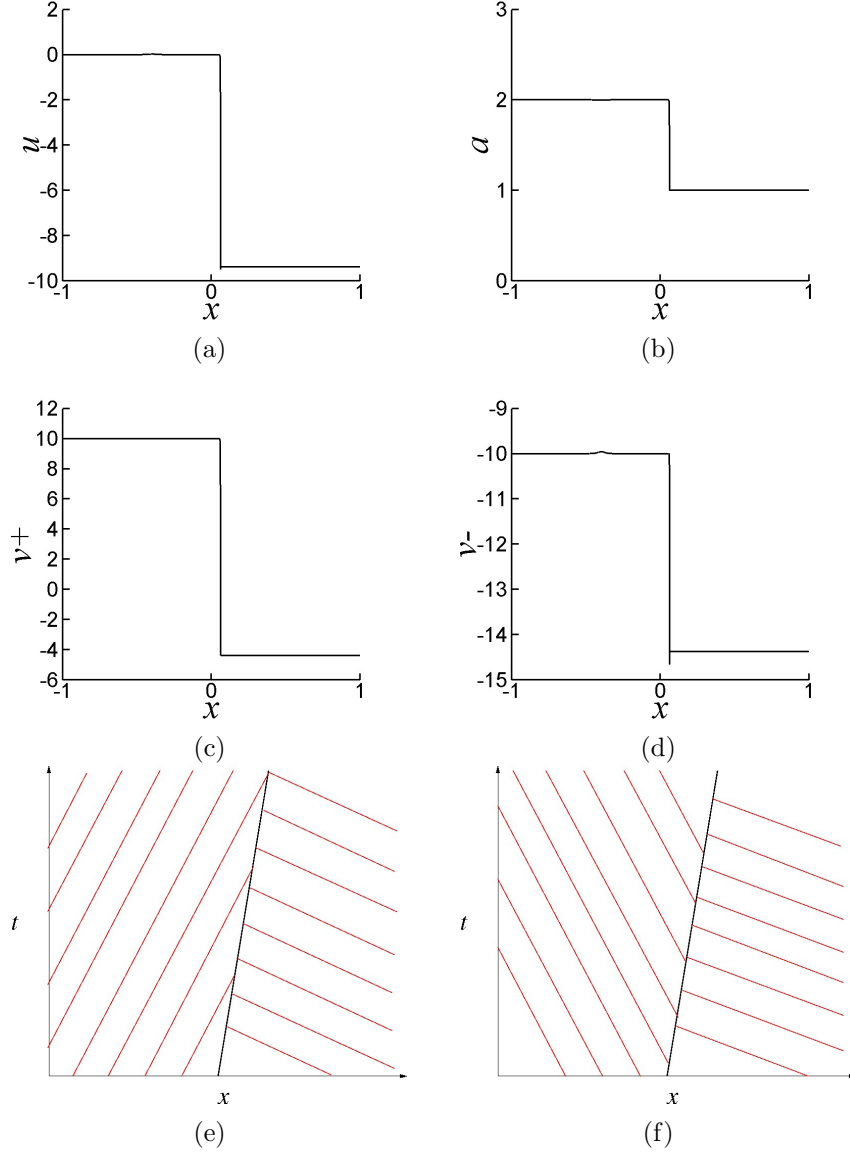


Figure 7: Example 3a at time $t = 0.2$. This example was chosen to have a single shock for the Homentropic Euler equations which is clearly visible in (a) and (b). The shock is moving to the right but clearly not as quickly as previous examples. (c) and (d) show the Riemann invariants v^+ and v^- . (e) and (f) are sketches of the characteristics for v^+ and v^- . Again in (f) v^- characteristics are being created at the shock.

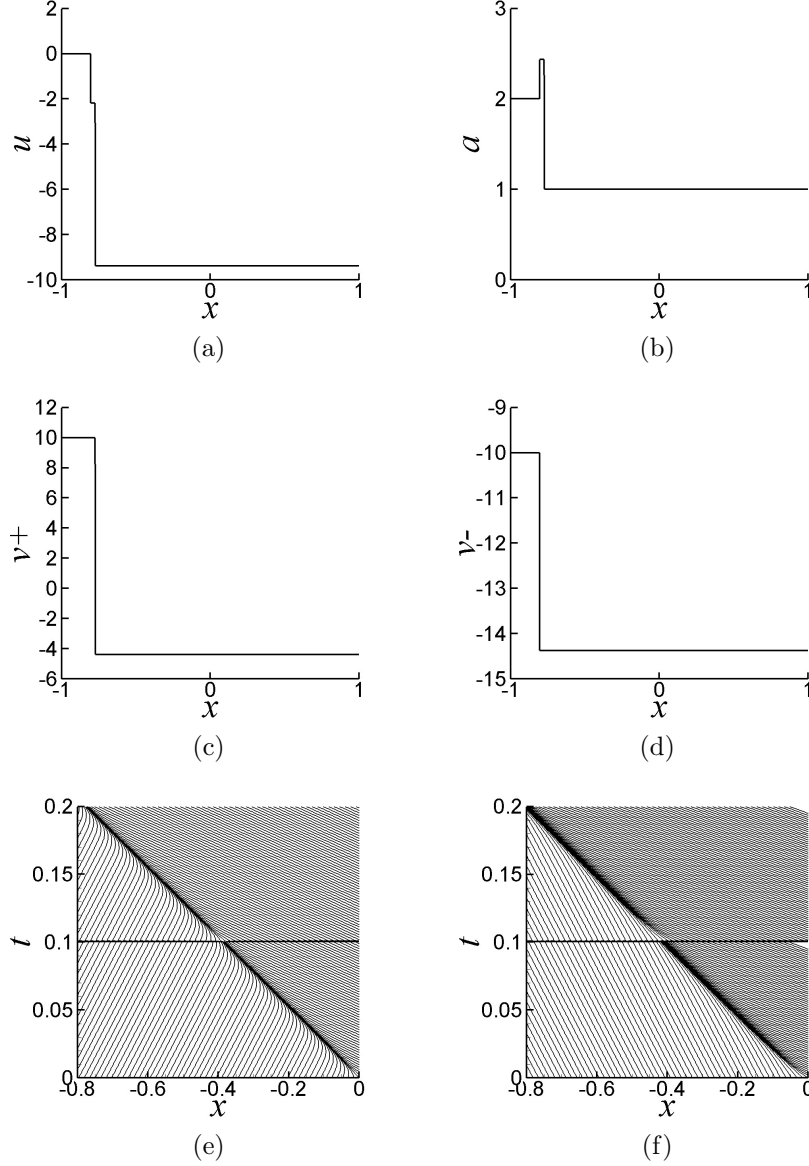


Figure 8: Example 3b at time $t = 0.2$ (a) and (b) show that there are two distinct left traveling shocks in the velocity and speed of sound. (c) and (d) show that these shocks exist separately in the Riemann invariants v^+ and v^- . (e) and (f) show the characteristics for v^+ and v^- . The horizontal line at time $t = 0.1$ represents the remapping of the simulation. In both (e) and (f) the characteristics are converging to the shocks, while never intersecting.